The Angular Correction Algorithm for the Intercalibration of Satellite Instruments Using CLARREO Pathfinder as a Reference

Wan Wu, Xu Liu, Qiguang Yang, Jon Chris Currey, Aron D. Bartle, Adam Thurston, Natividad M. Smith, Yolanda L. Shea, and Rajendra Bhatt

***Abstract*— The Climate Absolute Radiance and Refractivity (CLARREO) Pathfinder (CPF) mission will take Système Internationale (SI)-traceable spectral reflectance measurements of Earth at an unprecedented accuracy of 0.3% ($k = 1$). CPF will also take measurements to support intercalibration of other satellite-based sensors. To achieve the desired intercalibration methodology uncertainty of 0.3% ($k = 1$), the CPF intercalibration measurements need to closely match those from target sensors in time, space, angles, and wavelength. This article introduces an innovative angular correction method to significantly reduce errors due to angular mismatches between CPF and target sensor measurements. The method leverages the spectral correlations among the reflected solar (RS) radiances from the same surface target at two adjacent angles. Our studies have shown that the spectral radiance or reflectance difference measured at angles slightly deviating from the CPF observation angles can be accurately predicted based on the hyperspectral CPF measurements. The method will serve as part of the operational algorithms to support the core mission goal of conducting intercalibration analysis with measurements from the shortwave channel of the Clouds and the Earth's Radiance Energy System (CERES) and the reflective solar bands of the Visible Infrared Imaging Radiometer Suite (VIIRS); however, it can also be extended for other reference-target intercalibration applications.**

***Index Terms*— Angular correction, Climate Absolute Radiance and Refractivity (CLARREO) Pathfinder (CPF), climate benchmarking, intercalibration, Système Internationale (SI)-traceable.**

I. Introduction

THE Climate Absolute Radiance and Refractivity (CLARREO) Pathfinder (CPF) mission [1] began in 2016 and is designed to demonstrate essential measurement technologies required to obtain high-accuracy reflected solar (RS) climate observations. CPF includes an RS spectrometer that will be hosted on the International Space Station (ISS) for at least one year of operations. The CPF spectrometer will take highly accurate SI-traceable RS spectral reflectance measurements in the 350–2261 nm wavelength region, with a spectral sampling of 3 nm and a spectral resolution of 6 nm. The high accuracy CPF measurements will also serve as an intercalibration reference for other satellite-based RS sensors. Intercalibration ideally requires measurements to be matched in space, time, wavelength, and solar and view angles. However, finite differences in each of these dimensions are inevitable, so the CPF mission will also aim to limit intercalibration methodology uncertainty to 0.3% ($k = 1$, one sigma uncertainty or 68% confidence level). The intercalibration methodology uncertainty includes the uncertainty in the approaches used to mitigate spatial, temporal, spectral, and sun-view geometry differences between CPF as a reference and its intercalibration target sensors [2]. The CPF payload and the intercalibration sampling strategy have been carefully designed and optimized to minimize intercalibration sampling differences [3], but residual inconsistencies in these sampling domains may still introduce systematic errors that need to be corrected using specifically developed intercalibration algorithms.

CPF includes a two-axis pointing system that enables the boresight to be pointed along lines of sight within the field of view of target sensors with a maximum of a 10 min difference between CPF and target observations [1]. Wielicki et al. [2] briefly discussed the rationale that determines the temporal matching criteria which is interlinked with spatial matching requirement. However, there will still be differences in solar and viewing angles between CPF and target footprints. The difference in measurement time between CPF and target observations drives differences in solar zenith angle and solar azimuth angle (and therefore relative azimuth angle). Although the boresights of both instruments are closely matched in angle, the CPF, and target footprints will not necessarily be parallel, which can contribute to differences in viewing geometry (viewing zenith and viewing azimuth and therefore relative azimuth) if they are some distance away from the boresights. These sun-view geometry differences contribute to differences between the radiometric quantities measured by CPF and the target RS instrument. To meet the intercalibration methodology uncertainty of 0.3% ($k = 1$), this angular mismatch error, needs to be kept within 0.1% ($k = 1$).

This article characterizes the uncertainty attributed to potential angular mismatching differences associated with

Manuscript received 29 September 2023; revised 22 December 2023; accepted 20 January 2024. Date of publication 29 January 2024; date of current version 9 February 2024. This work was supported by the National Aeronautics and Space Administration Earth Science Division's CLARREO Pathfinder Project. *(Corresponding author: Wan Wu.)*

Wan Wu, Xu Liu, Jon Chris Currey, Yolanda L. Shea, and Rajendra Bhatt are with the National Aeronautics and Space Administration Langley Research Center, Hampton, VA 23681 USA (e-mail: wan.wu@nasa.gov).

Qiguang Yang is with ADNET Systems, Inc., Bethesda, MD 20817 USA.

Aron D. Bartle and Adam Thurston are with Mechdyne, Inc., Marshalltown, IA 50158 USA.

Natividad M. Smith is with Analytical Mechanics Associates, Inc., Hampton, VA 23666 USA.

Digital Object Identifier 10.1109/TGRS.2024.3359972

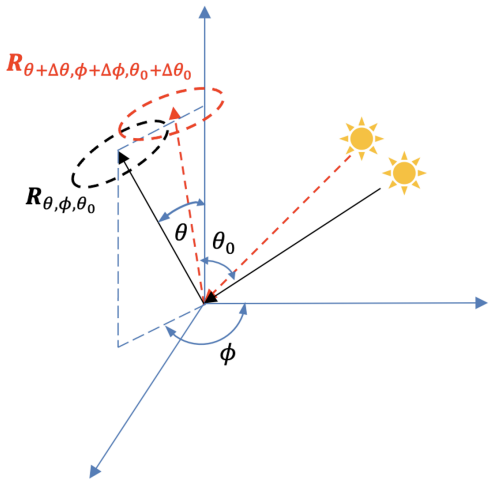

Fig. 1. Illustration of mismatched viewing and solar geometry vectors for CPF (black) and target (red) observations.

CPF-Clouds and the Earth's Radiance Energy System (CERES) and CPF-Visible Infrared Imaging Radiometer Suite (VIIRS) intercalibration and presents a methodology to reduce those errors with a correction (or adjustment). The study of CPF-CERES and CPF-VIIRS intercalibration events and the construction of the angular correction scheme are based on high accuracy, extensive, and low latency forward simulations. The principal component-based radiative transfer model (PCRTM) has been developed to address such needs [4], [5]. Details about the PCRTM-based simulations and the angular correction methodology are discussed. The CPF intercalibration high-fidelity simulation results are compared with real VIIRS and CERES data. The PCRTM-based intercalibration simulator estimates of potential angular mismatch error is also validated using the CERES measurement-based angular distribution models (ADMs) [6], [7], [8] to ensure that the angular difference used to evaluate the angular correction algorithm are sufficiently realistic. The efficacy of the angular correction algorithm, which is based on the spectral correlation relationships between observations at different angles, is demonstrated by applying it to an independently simulated hyperspectral radiance dataset.

II. Angular Correction Methodology

A. Overview

The purpose of this algorithm is to estimate the CPF spectral radiance for a given intercalibration sample (composite radiance value obtained by spatially convolving the CPF and target instrument observations over larger footprints within an intercalibration event), if CPF had the same sun-view geometry as the target sensor. The angular mismatch errors between CPF and target sensor observations over intercalibration samples can be represented by the arithmetic difference between observations that only differ by solar and viewing geometry. Fig. 1 illustrates an angular mismatch case between CPF and a target sensor. The difference in radiance observations can be characterized as a function of the CPF viewing zenith angle θ, solar zenith angle θ_0, relative azimuth angle ϕ, and the corresponding angular differences ($\Delta\theta$, $\Delta\theta_0$, and $\Delta\phi$) between the two observations, as follows:

$$\Delta \boldsymbol{R}_{\theta,\phi,\theta_0,\Delta\theta,\Delta\phi,\Delta\theta_0} = \boldsymbol{R}_{\theta+\Delta\theta,\theta_0+\Delta\theta_0,\phi+\Delta\phi} - \boldsymbol{R}_{\theta,\theta_0,\phi} \quad (1)$$

where $\boldsymbol{R}_{\theta,\theta_0,\phi}$ represents the CPF spectral radiance measured at θ, θ_0, and ϕ, and $\boldsymbol{R}_{\theta+\Delta\theta,\theta_0+\Delta\theta_0,\phi+\Delta\phi}$ represents the prediction of the CPF spectral radiance that could have been measured at $\theta + \Delta\theta, \theta_0+\Delta\theta_0$, and $\phi + \Delta\phi$. With $\boldsymbol{R}$ representing hyperspectral radiance signal of more than 600 channels, the relationship between $\Delta\boldsymbol{R}$ and $\boldsymbol{R}$ can be viewed as a spectrally dependent relationship. Such a relationship can be derived by quantifying the spectral correlation between $\Delta\boldsymbol{R}$ and $\boldsymbol{R}$ using a simple linear regression scheme

$$\Delta \boldsymbol{R}_{\theta,\phi,\theta_0,\Delta\theta,\Delta\phi,\Delta\theta_0} = \mathbf{A}_{\theta,\phi,\theta_0,\Delta\theta,\Delta\phi,\Delta\theta_0} \boldsymbol{R}_{\theta,\theta_0,\phi}. \quad (2)$$

$\boldsymbol{A}_{\theta,\phi,\theta_0,\Delta\theta,\Delta\phi,\Delta\theta_0}$ is the angular correction matrix that can be "trained" using preconstructed sample spectral radiances

$$\mathbf{A}_{\theta,\phi,\theta_0,\Delta\theta,\Delta\phi,\Delta\theta_0} = \left(\boldsymbol{R}_{\theta,\phi,\theta_0}\boldsymbol{R}^{T}_{\theta,\phi,\theta_0}\right)^{-1}\boldsymbol{R}_{\theta,\phi,\theta_0}\Delta\boldsymbol{R}^{T}_{\theta+\Delta\theta,\phi+\Delta\phi,\theta_0+\Delta\theta_0}. \quad (3)$$

The training data of $\boldsymbol{R}$ can be constructed via the PCRTM based high-fidelity radiative transfer simulations. PCRTM uses PC analysis to reduce the computational cost needed to simulate hyperspectral radiances by several orders of magnitude, while still maintaining the accuracy achieved by a line-by-line benchmark model [4], [5]. The simulated $\boldsymbol{R}_{\theta,\theta_0,\phi}$ can be well represented using a limited number of PCs (usually less than 100 PCs are needed, rather than the complete set of more than 600 PCs). Therefore, the dimension of $\mathbf{A}_{\theta,\phi,\theta_0,\Delta\theta,\Delta\phi,\Delta\theta_0}$ in (2) and (3) can be reduced by an order of magnitude and the risk of overfitting regression model is effectively prevented.

B. Constructing the Diverse Scene Hyperspectral Training Database for All Possible Sun-View Geometries

The angular correction relationship defined by $\mathbf{A}_{\theta,\phi,\theta_0,\Delta\theta,\Delta\phi,\Delta\theta_0}$ is scene dependent. $\mathbf{A}_{\theta,\phi,\theta_0,\Delta\theta,\Delta\phi,\Delta\theta_0}$ also needs to be established for the range of sun-view geometries possible during CPF intercalibration events. One year of CPF intercalibration event measurements are estimated to have millions of intercalibration samples. In order to practically obtain the angular correction relationship for each potential sample within a realistic time frame, we use a pre-constructed generalized database that stores simulated $\boldsymbol{R}$ for a variety of scene types measured at a wide range of sun-view geometry angles. The spectral training samples are stored in a database that consists of thousands of angular bins at discrete angles spanning the possible range of viewing geometry and solar angles of intercalibration events. Table I lists the discrete values associated with the angular bins stored in the database. Each angular bin of the database contains more than 11 000 simulated $\boldsymbol{R}_{\theta,\theta_0,\phi}$ associated with various scene types that may be observed during a CPF intercalibration event. The selection of the angular bin number is driven by the need to ensure accuracy in training spectral samples, particularly those not on angular grids, which require construction through interpolation among adjacent angular bins. We have done initial sensitivity test following

TABLE I
ANGULAR BIN INDEX VALUES OF THE REFERENCE DATA USED TO DERIVE THE ANGULAR CORRECTION RELATIONSHIP

θ = /	0.0, 5.0, 10.0, 15.0, 20.0, 25.0, 30.0, 32.5, 35.0, 37.5, 40.0, 42.5, 45.0, 47.5, 50.0, 52.5, 55.0, 57.5, 60.0, 62.5, 65.0 /
ϕ = /	0.0, 5.0, 10.0, 15.0, 20.0, 25.0, 30.0, 35.0, 40.0, 45.0, 50.0, 55.0, 60.0, 65.0, 70.0, 75.0, 80.0, 85.0, 90.0, 95.0, 100.0, 105.0, 110.0, 115.0, 120.0, 125.0, 130.0, 135.0, 140.0, 145.0, 150.0, 155.0, 160.0, 165.0, 170.0, 175.0, 180.0 /
θ_0 = /	0.0, 5.0, 10.0, 15.0, 20.0, 25.0, 30.0, 32.5, 35.0, 37.5, 40.0, 42.5, 45.0, 47.5, 50.0, 52.5, 55.0, 57.5, 60.0, 62.5, 65.0, 67.5, 70.0, 72.5, 75.0 /

* All values are in degrees

an experimental approach. We began with a 10° angular bin resolution for all three sun-view angles and assessed accuracy for spectral samples obtained via interpolation with sun-view angles 5° apart from adjacent bins. This involved comparing interpolated values with values directly simulated using exact angles. The resulting statistics, across various scene types, provided general guidance on achievable accuracy in different angular locations and for different scene types. Based on these statistics, we refined the angular bin resolution to 5° and subsequently to 2.5°. We conducted a similar accuracy validation study, with particular emphasis on scene types sensitive to angular changes in corresponding top of atmosphere (TOA) radiances. Our findings revealed that the gain in accuracy by improving angular resolution for solar and satellite angles below 30° was much smaller than the improvement achievable for cases with larger solar and satellite angles. The final choice, as indicated in Table I, reflects a balance between the accuracy of spectral radiance in training samples and considerations for the complexity and implementation efficiency of the angular correction approach based on the pre-constructed database.

The TOA radiance or reflectance spectrum of an observation is a function of various geophysical properties including absorbing gases, cloud properties (including cloud optical depth, height, physical thickness, and particle size), aerosol information (optical depth and mode), and surface bi-directional reflectance distribution function (BRDF). The input geophysical parameters used to calculate $\boldsymbol{R}_{\theta,\theta_0,\phi}$ for different scene types are extracted from a composite database. Cloud, aerosol, and surface reflectance parameters (over land) of this database are obtained from the Moderate Resolution Imaging Spectrometer (MODIS) Level 2 data products [9], [10], [11]. MODIS has 36 spectral measurement bands including one in the broad 6.7 μm water vapor absorption region and one in the 15 μm CO_2 absorption region [12]. The CO_2 and H_2O spectral bands give MODIS the edge over VIIRS for the retrieval of semitransparent ice cloud [13]. Temperature, precipitable water, O_3, and surface wind parameters (over ocean) are obtained from European Centre for Medium-Range Weather Forecasts (ECMWF) reanalysis data [14]. Considering the CPF intercalibration events are expected to occur within the 60°S–60°N latitude due to the orbital inclination of ISS, we populate our database using data spatially and temporally matched with randomly selected Aqua-MODIS observations of non-polar regions over different seasons of a year. Fig. 2 shows the geographic locations of the selected MODIS observations. This strategy aims to establish a reasonable space-time coverage for scene types anticipated during CPF intercalibration events.

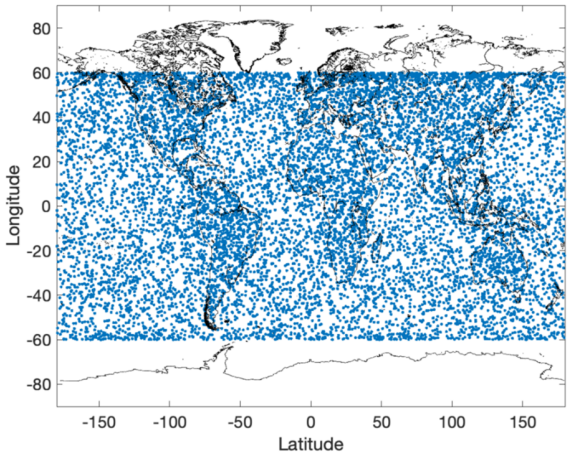

Fig. 2. Global distribution of the MODIS observations that serve as the reference dataset to generate the training spectra used in constructing the angular correction training database.

For a given scene type, the change of $\boldsymbol{R}_{\theta,\theta_0,\phi}$ within a small angular space spanning over a few degrees can be accurately represented as a simple function of $\Delta\theta$, $\Delta\theta_0$, and $\Delta\phi$. The training dataset for a given sun-view geometry that includes $\boldsymbol{R}_{\theta+\Delta\theta,\theta_0+\Delta\theta_0,\phi+\Delta\phi}$ and $\boldsymbol{R}_{\theta,\theta_0,\phi}$ can therefore be quickly obtained via an interpolation between the spectra from adjacent angular bins. Such a database-based approach enables a low latency implementation which is needed for its inclusion in the CPF data production pipeline.

C. Scene Identification

The construction of angular correction matrix **A** needs to be stratified for various scenes. There are different ways to stratify the scenes. A common method is to use geophysical parameters such as cloud, aerosol, and surface properties to stratify the scenes. These geophysical parameters can be obtained from the Level 2 data products of collocated imagers such as VIIRS. However, relying on external data products may impact the CPF data production timeline depending on the external data production latency. Moreover, potential intrinsic errors in those imager data products can introduce scene identification errors. Alternatively, the spectral shape and magnitude of CPF spectra are dependent on the underlying geophysical parameters, so the spectra can be used directly to stratify across various scenes. The hyperspectral measurements of CPF can capture fine spectral features imposed by different geophysical variables on the TOA radiances. This represents a significant advantage over broadband or multi-band sensors. Consequently, the measured CPF spectral radiances can be directly utilized to categorize scenes without resorting to auxiliary data. Therefore, we choose the low-latency approach that directly uses the spectral shape and magnitude of the calibrated CPF spectra for the scene stratification.

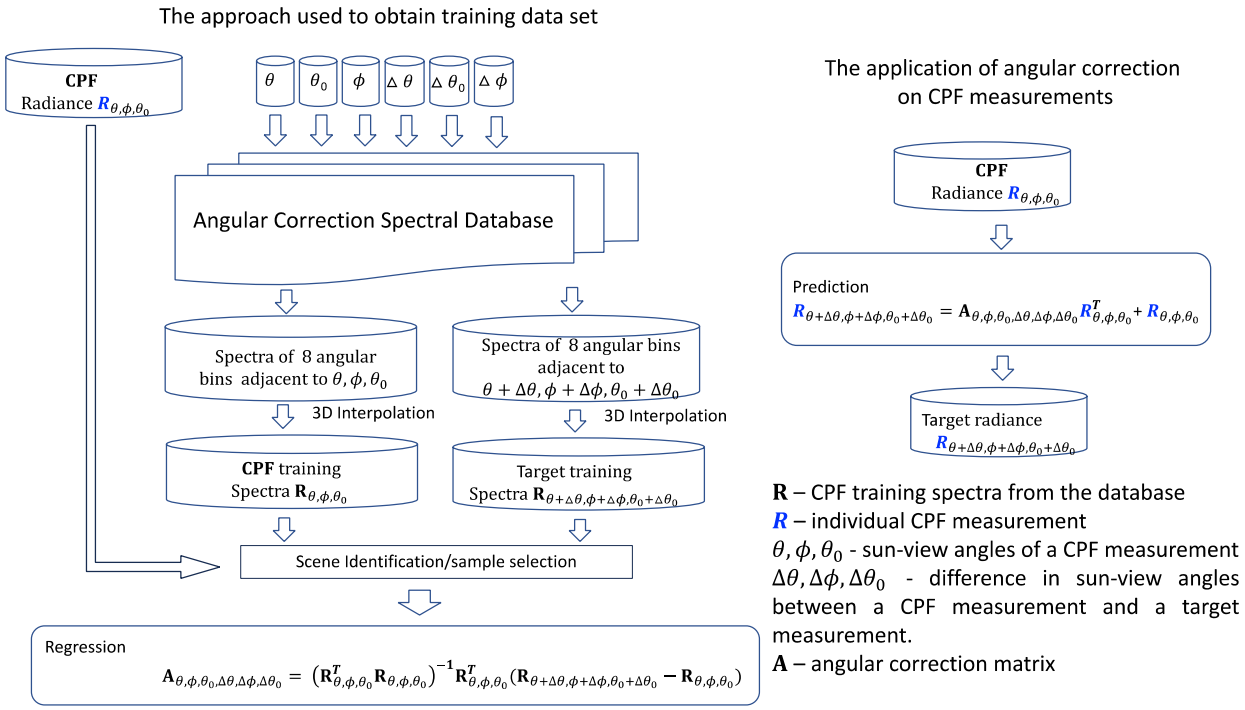

Fig. 3. Angular correction algorithm implementation flow diagram. (Left) Procedure used to obtain training dataset. (Right) Application of angular correction on a given CPF measurement.

Within the current angular correction approach, the angular correction matrix $\mathbf{A}$ for a given CPF spectral measurement is derived using spectral samples selected from the training spectral database. Only spectral samples that closely match the spectral shape and magnitude of the given CPF spectral measurement are selected from the database and used. In this way, the training samples used to derive $\mathbf{A}$ represent the same (or at least similar) scene type associated with the given observation. The selection of training samples is done via a spectral correlation analysis. More specifically, the degree of spectral correlation between the CPF measurement and a spectral sample from the database is quantified as the cosine of the angle between the two spectra

$$\cos\alpha = \frac{\boldsymbol{R}^{\boldsymbol{CPF}}_{\theta,\theta_0,\phi} \cdot \boldsymbol{R}^{\boldsymbol{training}}_{\theta,\theta_0,\phi}}{\|\boldsymbol{R}^{\boldsymbol{CPF}}_{\theta,\theta_0,\phi}\|\,\|\boldsymbol{R}^{\boldsymbol{training}}_{\theta,\theta_0,\phi}\|} \tag{4}$$

where $\boldsymbol{R}^{\boldsymbol{CPF}}_{\theta,\theta_0,\phi}$ represents the PC scores of the given CPF spectrum and $\boldsymbol{R}^{\boldsymbol{training}}_{\theta,\theta_0,\phi}$ represents the PC scores of the sample spectrum constructed from the database. After applying the spectral correlation analysis to all the sample spectra of the database, we select top 300 (out of total number of more than 11 000) training samples that provide the best match to $\boldsymbol{R}^{\mathbf{CPF}}_{\theta,\theta_0,\phi}$ (with the smallest $\cos\alpha$ values). The scene-dependent angular correction relationship $\mathbf{A}_{\theta,\phi,\theta_0,\Delta\theta,\Delta\phi,\Delta\theta_0}$ can therefore be constructed based on the $\boldsymbol{R}_{\theta+\Delta\theta,\theta_0+\Delta\theta_0,\phi+\Delta\phi}$ and $\boldsymbol{R}_{\theta,\theta_0,\phi}$ corresponding to those 300 spectral samples. The $\cos\alpha$ factor can be used as a quality control factor that reflects the representativeness of specific scene types in the database training samples.

D. Implementation Scheme

Fig. 3 shows a flow diagram that illustrates the implementation of the angular correction algorithm. CPF provides spectral reflectance and radiance measurements [1]. Angular correction is applied to the CPF spectral radiances. In order to facilitate the implementation and avoid potential inconsistency between the solar irradiance currently used by the PCRTM simulation (Kurucz [15]) and that to be used to generate CPF radiance (TSIS-1 [16]), we save spectral reflectance values in the spectral sample database used for the construction of the angular correction regression matrix. TSIS-1 solar irradiance can therefore be used to convert PCRTM calculated reflectance spectra ρ back into radiance $\boldsymbol{R}$.

The PCRTM-calculated spectral samples are extracted from the database using the corresponding sun-view geometries defined by θ, θ_0, ϕ, $\Delta\theta$, $\Delta\theta_0$, and $\Delta\phi$. This step involves a 3-D interpolation to compute spectral radiances at the specific CPF and target angles. The training spectral radiance datasets are refined following the scene identification approach discussed in Section II-C. After deriving $\mathbf{A}$ via a linear regression analysis, the spectral radiance at the target's sun-view geometry, $\boldsymbol{R}_{\theta+\Delta\theta,\theta_0+\Delta\theta_0,\phi+\Delta\phi}$, is obtained by using (2). It is noted here that the output from the angular correction algorithm needs to be integrated with other intercalibration methodologies developed to improve the spatial, temporal, and spectral matching between measurements of CPF and target sensors. However, those topics are beyond the scope of this article and will not be discussed here.

III. Validation of the Angular Correction Algorithm

The validation of the angular correction algorithm primarily relies on simulation-based results, considering the absence of benchmark observation-based data suitable for this purpose. The validation work consists of three parts: 1) constructing high-fidelity data that can closely mimic

the CPF inter-calibration events and, therefore, be used to characterize the realistic angular mismatch errors; 2) validating the simulated angular mismatch error estimates using results from an independent approach; and 3) validating the regression-prediction-based angular correction scheme defined in Section II.

A. Intercalibration Event Simulation via PCRTM-Based High-Fidelity Simulator

The CPF intercalibration team has developed a sophisticated intercalibration high-fidelity simulator (HFS) to generate proxy data for conducting pre-launch algorithm studies and validation [17]. The HFS comprises several components, including the intercalibration event prediction, the generation of geophysical parameters associated with CPF, VIIRS, and CERES observations within each intercalibration events, the forward simulation to generate radiance and reflectance measured by CPF, VIIRS, and CERES.

The event predictor of the HFS provides geolocation and sun-view geometry angles for CPF, VIIRS, and CERES observations during each intercalibration opportunity [3]. Fig. 4 shows the geolocation of simulated intercalibration events between CPF and CERES/VIIRS aboard the Suomi National Polar-orbiting Partnership (SNPP) satellite from the HFS for January 2017. This one-month dataset includes 109 intercalibration events, encompassing approximately 70 000 CPF-VIIRS samples and over 44 000 CPF-CERES samples. Each CPF-VIIRS sample comprises a 15 × 15 km footprint, containing hundreds of CPF and VIIRS pixels. Similarly, each CPF-CERES sample comprises a CERES footprint and the CPF pixels located within it.

The geophysical parameters assigned to CPF-VIIRS intercalibration pixels are derived from VIIRS Level 2 products and ECMWF reanalysis data. These parameters are spatially and temporally matched to the time and geolocations generated by the event predictor. The spatial interpolation is done using nine nearest neighbor values following an inverse distance method. More specifically, geophysical parameters including aerosol optical thickness (AOT), precipitable water, and total column ozone, are extracted from the SNPP VIIRS NASA standard Level-2 (L2) Deep Blue aerosol product (AERDB_L2_VIIRS_SNPP) product that has a 6 × 6 km spatial resolution at nadir and a 6 min temporal resolution [18]. Cloud properties including optical thickness, phase, particle size, height, and cloud mask are sourced from the SNPP VIIRS incarnation of the cloud properties continuity product (CLDPROP_L2_VIIRS_SNPP) with its temporal and horizontal resolution defined by the VIIRS measurements of moderate resolution band (6 min and 750 m) [19]. BRDF parameters are derived from daily global VIIRS BRDF product (VNP43C1) [20]. Temperature data required for simulating CERES IR radiances are extracted from 0.5° × 0.5° 3-h ECMWF Reanalysis-Interim (ERA-Interim) results [14].

The parameters matched to CPF and VIIRS pixels are fed to the forward simulation module of HFS, where PCRTM is used to simulate corresponding CPF-like spectra data for each pixel within an inter-calibration footprint. Spectral radiances

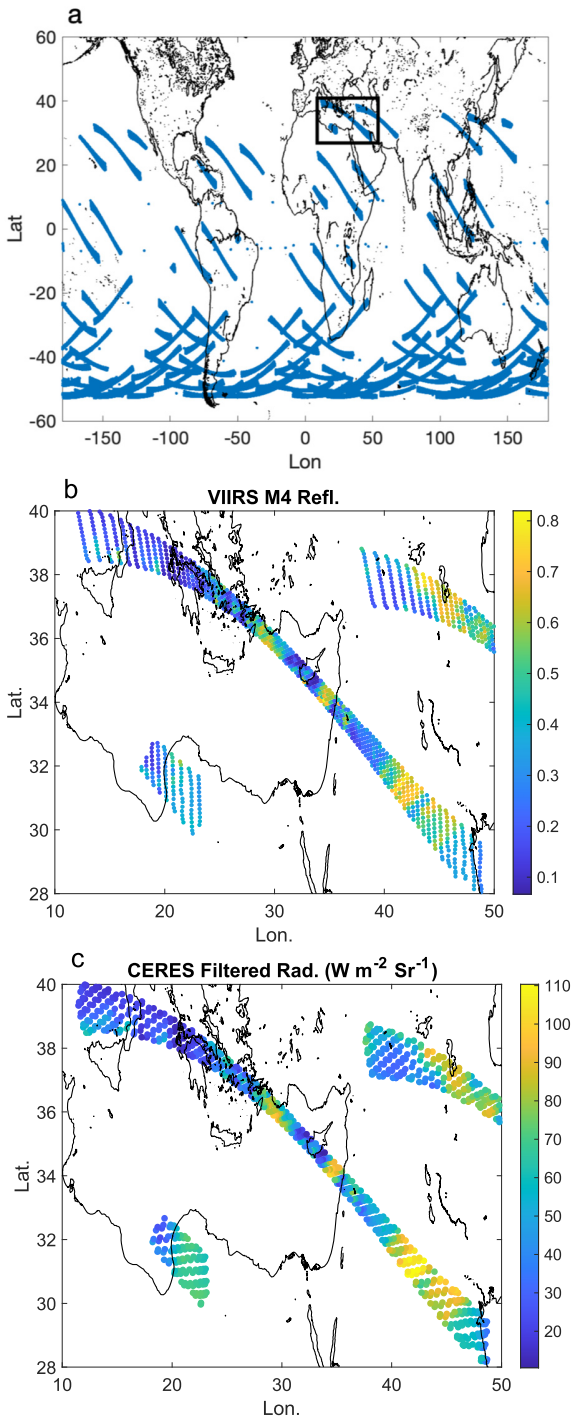

Fig. 4. (a) Locations of SNPP-ISS intercalibration events for January 2017 from the event simulator. (b) CPF-VIIRS intercalibration footprints of selected simulated intercalibration events [see locations highlighted in (a)]. (c) CPF-CERES intercalibration samples.

of CPF-VIIRS inter-calibration pixels within a 15 × 15 km footprint are converted into VIIRS band reflectance following a spectral and spatial matching procedure. To generate VIIRS reflectance data, CPF spectral radiances are convolved with the spectral response functions (SRFs) of VIIRS bands, yielding band radiances. These band-integrated radiances are then converted to reflectances using corresponding band-specific convolved solar irradiances. CERES broadband radiance data

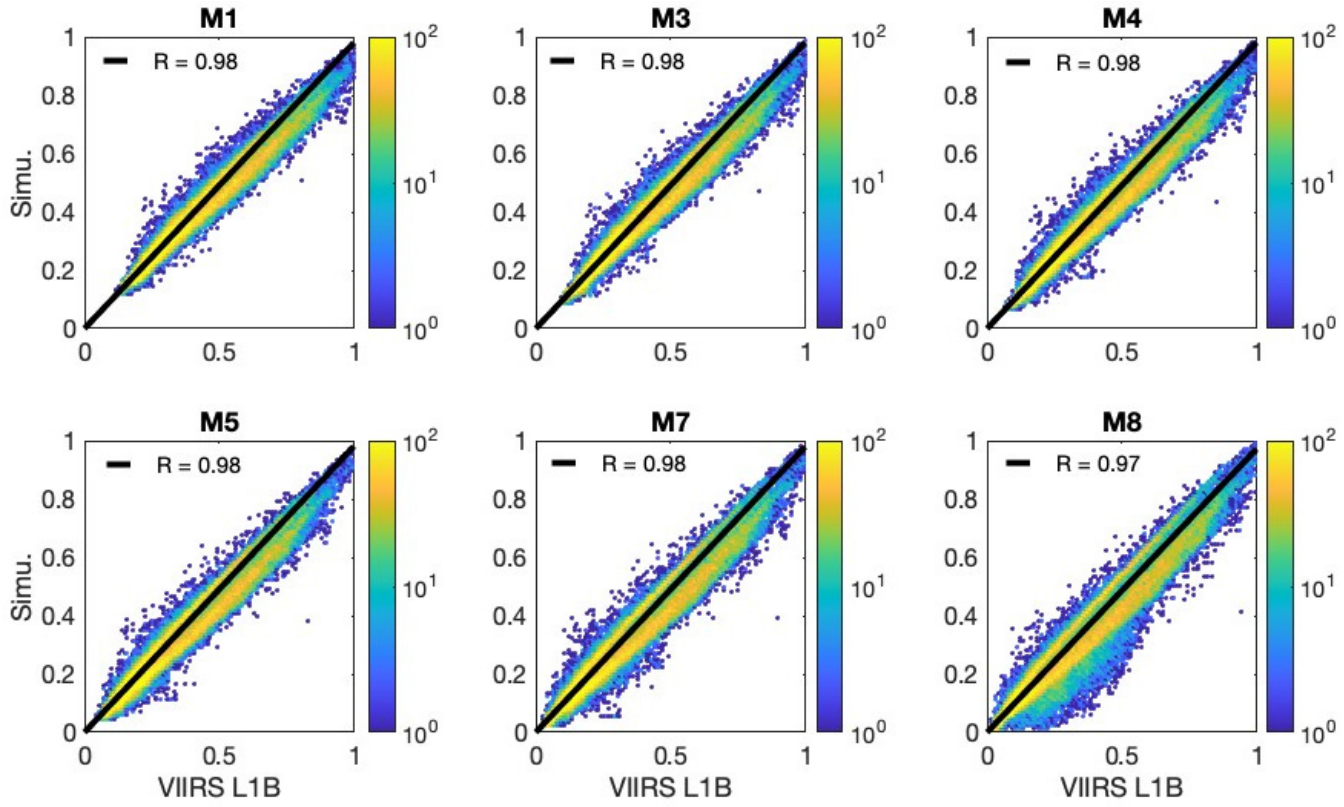

Fig. 5. Inter-comparison between VIIRS reflectance of select bands from the L1B product and the high-fidelity simulation results.

for a CPF-CERES footprint is generated by integrating CPF spectral radiances for each CPF pixel and then spatially convolving all pixel radiances within the CERES footprint with the CERES point spread function. The simulation of CERES-like broadband measurements also requires the filling of missing measurements in ultraviolet (UV) and infrared spectral region outside of CPF measurement scope, a procedure called "spectral band extension (or spectral gap filling)." The spectral band extension algorithm utilizes pre-established spectral correlation relationships among wavelengths to extend the CPF spectrum below 350 nm and above 2300 nm [21].

The results from HFS are first validated using the real VIIRS reflectance and CERES radiance. Fig. 5 compares the simulated VIIRS reflectance of different moderate resolution bands with data from the SNPP platform-based NASA VIIRS Level 1B radiance/reflectance product (VNP02MOD) for the inter-calibration footprints shown in Fig. 4 [22]. Similarly, Fig. 6 compares the simulated short-wave radiances of CPF-CERES footprints with those from the CERES Single Scanner Footprint TOA/Surface Fluxes and Clouds (SSF) product [23]. The scatter plots in both Figs. 5 and 6 demonstrate a general agreement between the HFS results and real VIIRS and CERES data products.

Besides potential forward model errors, major difference between HFS results and observations shown in Figs. 5 and 6 are due to potential errors in input parameters that include atmospheric, cloud, aerosol, and surface properties used for the forward simulation. These errors can originate from data sources, or be introduced by the spatiotemporal interpolation

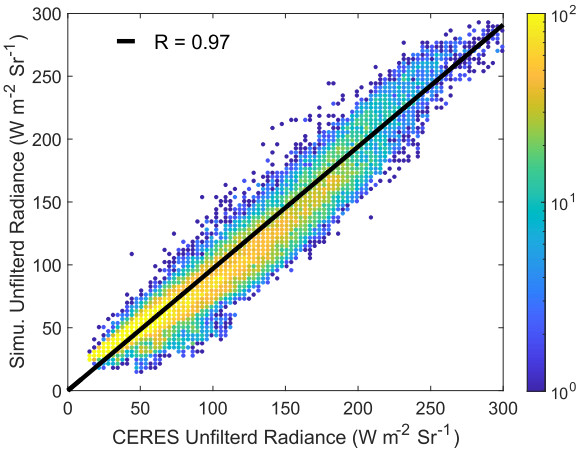

Fig. 6. Inter-comparison between CERES unfiltered radiances from the SSF product and the HFS results.

employed to match the pixels within inter-calibration footprints. However, the systematic bias of the difference is reasonably small with relative errors ranging within a few percent. The simulation results are well correlated with the real data in both Figs. 5 and 6, which justifies the 'high-fidelity' feature of the HFS to capture the scene variations in the real observations. It is noted that HFS is used to emulate the characteristics of real observations that has a potential impact on the performance of inter-calibration algorithms. The characterization for the angular mismatch error depends on how accurately HFS captures the underlying scene anisotropy

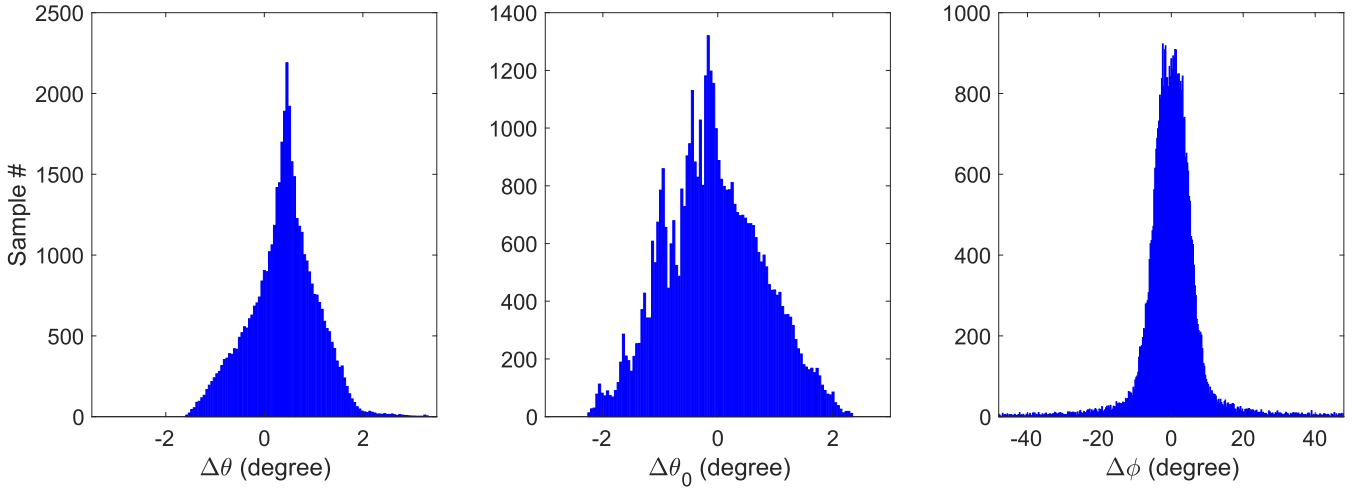

Fig. 7. Angular mismatch between CPF and CERES for the intercalibration events in January 2017.

associated with real measurements, and not solely determined by the HFS accuracy demonstrated in Figs. 5 and 6. Further validation of the simulation of angular mismatch error using HFS is presented in Section III-B through an additional study.

B. Intercomparison Between PCRTM- and CERES ADM-Based CPF-CERES Angular Mismatch Errors

CERES ADMs have been developed to facilitate the conversion of broadband radiance measurements into TOA fluxes. These ADMs are constructed by sorting mean radiances and corresponding upwelling fluxes into angular bins for stratified scene types. For a given scene type, the ADM radiances associated with different angular bins can be used to quantify the angular relationship between broadband measurements at different viewing geometry angles. The CPF-CERES angular mismatch error simulated using the HFS can therefore be validated using the anisotropic factor derived from CERES ADMs. The CERES ADMs Edition 4 are used here for the validation of HFS results [6], [7], [8].

The geolocation and observation times for the January 2017 intercalibration events shown in Fig. 4 correspond to real CERES observations. Therefore, we can derive the angular mismatch error for each intercalibration sample based on the sun-view geometry angles and scene types identified using the CERES ADMs. Fig. 7 shows the histograms illustrating the differences between CPF and CERES sun-view geometry angles for the intercalibration events in January 2017. There is a 0.38° systematic bias in $\Delta\theta$, a $-0.06°$ bias in $\Delta\theta_0$, and a $-0.21°$ bias in $\Delta\phi$. These biases imply that the CPF-CERES angular mismatch errors cannot be simply averaged out by using a large number of intercalibration samples. Based on those sun-view geometry angles, the HFS produces two sets of CERES radiance results for all CPF-CERES intercalibration footprints, as depicted in Fig. 4(a). These two sets of results are simulated using the same geophysical parameters assigned to the CPF pixels, extracted from VIIRS Level 2 data, and matched to CPF pixels through spatial interpolation. The difference between two sets of results yields a 0.11% bias. Using the same sun-view angles, we can also evaluate the

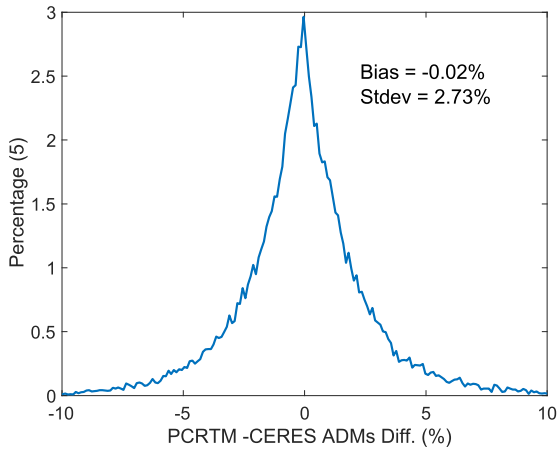

Fig. 8. Probability distribution of the difference between the angular mismatch errors from the PCRTM HFS and from the CERES ADMs.

angular mismatch error using the anisotropic factors from the CERES ADMs. The anisotropic factors define the relative difference between the broadband radiances measured by CERES at different sun-view geometries. The statistical bias based on the CERES ADMs is 0.13%. A systematic error larger than 0.1% due to the angular difference alone is deemed as significant.

Fig. 8 further illustrates the distribution of the difference between angular mismatch errors from the HFS and from the CERES ADMs. The distribution shows an excellent agreement (mean difference of 0.02%) between the mismatch error estimates from the two independent approaches. The standard deviation (σ) of the difference is ~2.73%, which indicates a smaller than 0.01% uncertainty associated with the systematic difference (being evaluated as $\sigma(N)^{1/2}$ following the central limit theorem with N being the number of samples that is larger than 44 000). The agreement between simulation results and the independent CERES ADM results confirms that underlying scene reflectance anisotropy difference between the CPF and target instruments can be accurately quantified using the HFS. The results shown in Figs. 5, 6, and 8 together support the suitability of using the PCRTM-based HFS as

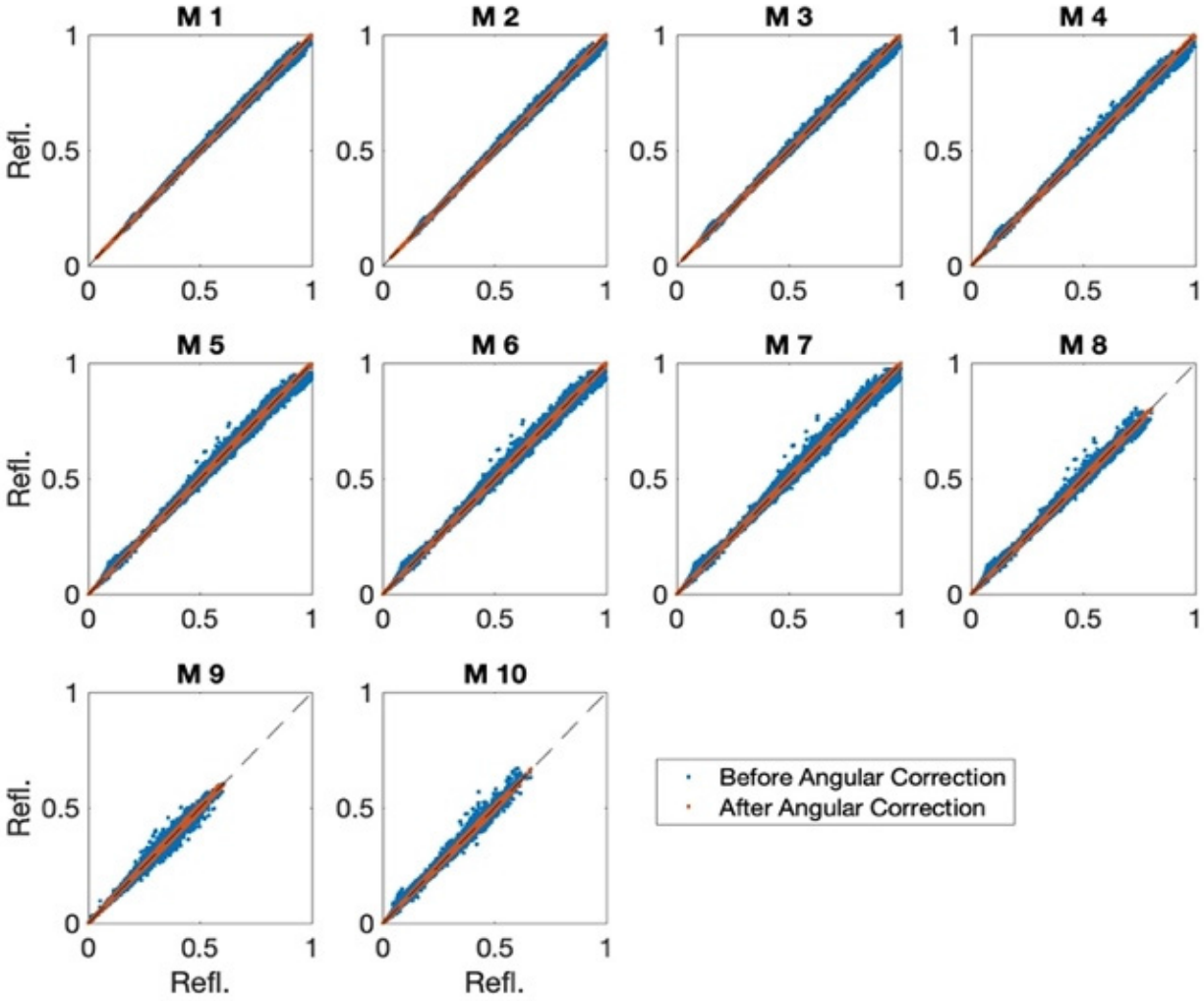

Fig. 9. VIIRS reflectance established from the simulated CPF radiances before (blue) and after (red) the angular correction. x-axis represents the VIIRS reflectance directly simulated.

a viable proxy to evaluate the performance of the angular correction algorithm in support of CPF-CERES and CPF-VIIRS intercalibration.

C. Validation of the Database-Based Regression-Prediction Approach Used for the Angular Correction

The database-based angular correction scheme, as described in Section II, is validated using the HFS results for the intercalibration events (shown in Fig. 4) under a perfect spectral and spatial sampling condition. The simulation study is designed to exclude any CPF-CERES or CPF-VIIRS difference due to causes other than angular mismatch. For each 15 $\times$ 15 km footprint of the CPF-VIIRS intercalibration events, the spectral radiances of CPF pixels within the footprint observed at sun-view geometry angles of both CPF and VIIRS are simulated. The resulting sets of simulated pixel radiances, corresponding to CPF and VIIRS sun-view geometry angles, are converted to VIIRS band reflectances following the spectral-spatial matching procedure outlined in Section III-A. A comparison is then made between these two sets of reflectance data to quantify CPF-VIIRS angular difference effects. Similarly, the evaluation of CPF-CERES angular mismatch error involves the comparison between two sets of broadband radiances generated using the CPF spectral radiances simulated for the same pixels but at CPF and CERES sun-view geometry angles, respectively. Inter-calibration errors originated from factors such as the uncertainty in VIIRS SRF or CERES point spread function are not included in the simulation.

The blue dots in Figs. 9 and 10 illustrate simulated CPF-VIIRS and CPF-CERES difference due to the angular mismatch for SNPP-ISS intercalibration events for January 2017 following the HFS procedure described here. Fig. 9 illustrates the effectiveness of the angular correction algorithm in reducing the difference between VIIRS and CPF reflectance values caused by the angular mismatch. The plot exhibits an obvious dispersion between VIIRS and CPF reflectance values before correction (depicted by blue dots). However, after implementing the angular correction, the dispersion (depicted by red points) is significantly reduced, indicating an excellent agreement between two sets of reflectance data. Similarly, the effectiveness of the angular correction algorithm in mitigating

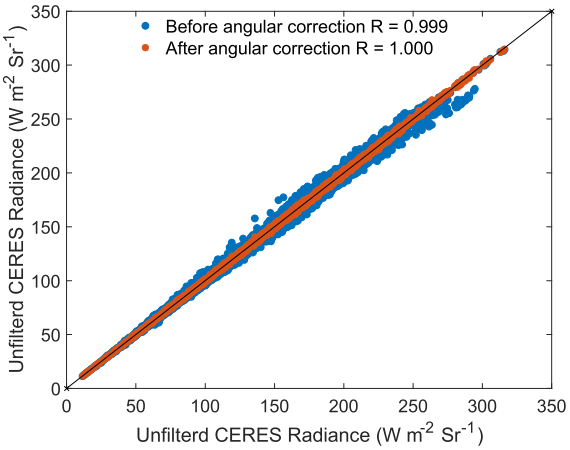

Fig. 10. CERES unfiltered radiances computed from the simulated CPF radiances before (blue) and after (red) the angular correction. The x-axis represents the directly simulated CERES unfiltered radiances.

TABLE II
ANGULAR MISMATCH ERRORS BEFORE AND AFTER CORRECTION

	Bias		Standard Deviation	
	Before Correction	After Correction	Before Correction	After Correction
VIIRS				
M1	0.19 %	-0.01 %	1.03 %	0.25 %
M2	0.18 %	-0.01 %	1.12 %	0.30 %
M3	0.18 %	-0.01 %	1.29 %	0.36 %
M4	0.16 %	-0.02 %	1.57 %	0.46 %
M5	0.17 %	-0.02 %	1.93 %	0.55 %
M6	0.18 %	-0.02 %	2.07 %	0.59 %
M7	0.18 %	-0.02 %	2.21 %	0.62 %
M8	0.19 %	-0.02 %	2.36 %	0.66 %
M9	0.03 %	-0.05 %	2.74 %	1.22 %
M10	0.25 %	-0.03 %	2.96 %	0.99 %
CERES	0.11 %	-0.01 %	1.87 %	0.65 %

the CPF-CERES angular difference is demonstrated in Fig. 10.

Table II lists the statistical bias and the standard deviation (σ) of angular mismatch errors in the comparison of VIIRS reflectance and CERES radiances. Also listed are the corresponding values for the remaining errors after the angular correction. Before implementing the angular correction algorithm, both CPF-VIIRS and CPF-CERES cases exhibited angular mismatch systematic errors that could potentially reach up to 0.25%, surpassing the required threshold of 0.1%. After implementation of the angular correction, the remaining systematic errors are now comfortably below 0.1%. Additionally, the standard deviation of the residual errors has notably decreased following the angular correction. Based on our sampling analysis, we anticipate a monthly intercalibration sample size exceeding 5000 for both CERES and VIIRS. As such, the combined quadrature sum of systematic error and random uncertainty (being evaluated as $\sigma/(5000)^{1/2}$ following the central limit theorem) can be maintained well below 0.1% following the implementation of the angular correction.

IV. CONCLUSION

The CPF hyperspectral measurements enable us to leverage the spectral correlation relationship to account for differences between observations acquired at slightly different sun-view geometries. The angular correction relationship can be characterized using pre-constructed spectral samples that correspond to a wide range of scenes and are sorted by different angular bins. These training spectral samples are calculated using PCRTM. Although it is challenging to emulate real measurements with simulations at a high accuracy, the validation study conducted utilizing the real CERES and VIIRS observation data demonstrates that the scene-dependent variations can be effectively captured by the PCRTM-based simulations. Most importantly, the angle-dependent spectral difference can be accurately quantified using the simulation results.

The PCRTM-based HFS has been employed to estimate the potential angular mismatch error and validate the angular correction algorithm. The estimated angular mismatch errors derived from HFS align with the results obtained from CERES ADMs. The analysis of one month of simulated intercalibration events demonstrates that, without correction, the CPF-CERES intercalibration errors due to the angular mismatch can exceed 0.1%, which exceeds the CPF-CERES angular correction requirement needed to fit within the 0.3% CPF intercalibration methodology uncertainty. The intercomparison study between the CERES ADMs and the HFS results demonstrates a remarkable agreement (with a mean difference of only 0.02%) in the estimates of mismatch errors, thereby reaffirming the reliability and precision of the PCRTM-based HFS method in quantifying underlying scene reflectance anisotropy differences for satellite intercalibration. The validation study using HFS results shows that the regression-prediction based angular correction algorithm can effectively reduce errors within individual footprints of different scenes, thereby substantially removing the systematic bias resulting from angular mismatch errors. The magnitude of the residual error after correction based on one month of intercalibration samples from HFS falls within the CPF intercalibration angular correction algorithm's stipulated uncertainty requirement of 0.1%.

ACKNOWLEDGMENT

The authors really appreciate the advice and support provided by the CERES ADM working group.

REFERENCES

[1] Y. Shea et al., "Clarreo pathfinder: Mission overview and current status," in *Proc. IEEE Int. Geosci. Remote Sens. Symp. (IGARSS)*, Waikoloa, HI, USA, Sep. 2020, pp. 3286–3289.

[2] B. A. Wielicki, D. R. Doelling, D. F. Young, N. G. Loeb, D. P. Garber, and D. G. MacDonnell, "Climate quality broadband and narrowband solar reflected radiance calibration between sensors in orbit," in *Proc. IEEE Int. Geosci. Remote Sens. Symp. (IGARSS)*, Jul. 2008, pp. I257–I260.

[3] C. M. Roithmayr et al., "CLARREO approach for reference intercalibration of reflected solar sensors: On-orbit data matching and sampling," *IEEE Trans. Geosci. Remote Sens.*, vol. 52, no. 10, pp. 6762–6774, Oct. 2014.

[4] X. Liu et al., "Development of a fast and accurate PCRTM radiative transfer model in the solar spectral region," *Appl. Opt.*, vol. 55, no. 29, p. 8236, 2016.

[5] Q. Yang, X. Liu, W. Wu, S. Kizer, and R. R. Baize, "Fast and accurate hybrid stream PCRTM-SOLAR radiative transfer model for reflected solar spectrum simulation in the cloudy atmosphere," *Opt. Exp.*, vol. 24, no. 26, pp. A1514–A1527, 2016.

[6] J. Corbett and W. Su, "Accounting for the effects of sastrugi in the CERES clear-sky Antarctic shortwave angular distribution models," *Atmos. Meas. Techn.*, vol. 8, no. 8, pp. 3163–3175, Aug. 2015.

[7] W. Su, J. Corbett, Z. Eitzen, and L. Liang, "Next-generation angular distribution models for top-of-atmosphere radiative flux calculation from CERES instruments: Methodology," *Atmos. Meas. Techn.*, vol. 8, no. 2, pp. 611–632, Feb. 2015.

[8] W. Su, J. Corbett, Z. Eitzen, and L. Liang, "Next-generation angular distribution models for top-of-atmosphere radiative flux calculation from CERES instruments: Validation," *Atmos. Meas. Techn.*, vol. 8, no. 8, pp. 3297–3313, Aug. 2015.

[9] MODIS, "MODIS atmosphere L2 cloud product (MOD06)," NASA Earthdata, Washington, DC, USA, Tech. Rep. MOD06_L2.006, 2023, doi: 10.5067/MODIS/ MOD06_L2.006.

[10] R. Levy and C. Hsu, "MODIS atmosphere L2 aerosol product. NASA MODIS adaptive processing system," Goddard Space Flight Center, Greenbelt, MD, USA, Tech. Rep. MYD04_L2.006, 2015, doi: 10.5067/MODIS/MYD04_L2.006.

[11] MODIS Land Science Team, "The moderate resolution imagingspectroradiometer (MODIS) MCD43A2 Version 6.1 bidirectional reflectance distribution function and albedo (BRDF/Albedo)," NASA, Earthdata, Washington, DC, USA, Tech. Rep. MCD43A2.061, 2023, doi: 10.5067/MODIS/MCD43A2.061.

[12] W. L. Barnes, T. S. Pagano, and V. V. Salomonson, "Prelaunch characteristics of the moderate resolution imaging spectroradiometer (MODIS) on EOS-AM1," *IEEE Trans. Geosci. Remote Sens.*, vol. 36, no. 4, pp. 1088–1100, Jul. 1998.

[13] B. A. Baum et al., "MODIS cloud-top property refinements for collection 6," *J. Appl. Meteorol. Climatol.*, vol. 51, no. 6, pp. 1145–1163, Jun. 2012.

[14] ECMWF Interim Reanalysis (ERA-Interim). *European Centre for Medium-Range Weather Forecasts*. [Online]. Available: https://www.ecmwf.int/en/forecasts/datasets/

[15] R. L. Kurucz, "New atlases for solar flux, irradiance, central intensity, and limb intensity," *Memorie della Societ Astronomica Italiana Suppl.*, vol. 8, p. 189, 2005.

[16] *Total and Spectral Solar Irradiance Sensor 1 (TSIS-1)*, Nat. Aeronaut. Space Admin. (NASA), 2017. [Online]. Available: https://www.nasa.gov/tsis-1

[17] W. Wu et al., "Development of a high-fidelity clarreo pathfinder simulator," in *Proc. IEEE Int. Geosci. Remote Sens. Symp.*, 2020, pp. 6385–6388, doi: 10.1109/IGARSS39084.2020.9323331.

[18] S. Platnick et al., "VIIRS atmosphere L2 cloud properties product. Version-1," NASA Level-1 Atmos. Arch. Distrib. Syst. (LAADS) Distrib. Act. Arch. Center (DAAC), Goddard Space Flight Center, Greenbelt, MD, USA, Tech. Rep. CLDPROP_L2_VIIRS_SNPP.001, 2017, doi: 10.5067/VIIRS/CLDPROP_L2_VIIRS_SNPP.001.

[19] C. Hsu, "The Deep Blue aerosol project: Aerosol retrievals from VIIRS," NASA Level-1 and Atmosphere Archive & Distribution System (LAADS) Distributed Active Archive Center (DAAC), Goddard Space Flight Center, Greenbelt, MD, USA, Tech. Rep., 2018, doi: 10.5067/VIIRS/AERDB_L2_VIIRS_SNPP.002.

[20] C. Schaaf, Z. Wang, X. Zhang, and A. Strahler, *VIIRS/NPP BRDF/Albedo Albedo Model Parameters Daily L3 Global 0.05 Deg CMG V001*, document VNP43C1v001, NASA EOSDIS Land Processes Distributed Active Archive Center, 2019, doi: 10.5067/VIIRS/VNP43C1.001.

[21] Q. Yang, X. Liu, and W. Wu, "Extending Spectral range of clarreo-pathfinder for ceres intercalibration," in *Proc. AGU Amer. Geophys. Union Fall Meeting*, San Francisco, CA, USA, 2019, pp. A33L–2949.

[22] N. Baker, *VIIRS Radiometric Calibration Algorithm Theoretical Basis Document (ATBD)*, document 432-ATBD-001, Goddard Space Flight Center, NASA, Greenbelt, MD, USA, 2014. [Online]. Available: https://ncc.nesdis.noaa.gov/documents/documentation/gsfc-474-00027-jpss-npp-viirs-radiometric-calibration-atbd–alt.-doc.-no.-d43777-.pdf

[23] N. Loeb, N. Manalo-Smith, W. Su, M. Shankar, and S. Thomas, "CERES top-of-atmosphere Earth radiation budget climate data record: Accounting for in-orbit changes in instrument calibration," *Remote Sens.*, vol. 8, no. 3, p. 182, Feb. 2016.

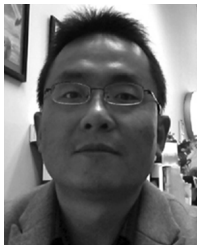

Wan Wu received the Ph.D. degree in physics from the University of Florida, Gainesville, FL, USA, in 2007.

He is currently a Research Physical Scientist with the NASA Langley Research Center, Hampton, VA, USA. His graduate school research work focused on the design and development of the input optics subsystem for the laser interferometer and gravitational-wave observatory project. After graduation, he has worked on numerous atmospheric remote sensing projects, taking different roles from instrument engineering to data processing algorithm development. At the NASA Langley Research Center, he has worked on the development of the principal components radiative transfer model, the retrieval algorithm development for various hyperspectral sounder missions, including National Airborne Sounder Testbed Interferometer, Infrared Atmospheric Sounding Interferometer, Atmospheric InfraRed Sounder, Cross-track Infrared Sounder, the instrument design trade study for the Climate Absolute Radiance and Refractivity Observatory (CLARREO) mission, and the intercalibration algorithm development for CLARREO Pathfinder project. His research interests include the exploration of novel approaches of using remote sensing data in weather and climate study.

Xu Liu received the Ph.D. degree in physical chemistry from the University of Denver, Denver, CO, USA, in 1989.

He is currently a Physical Scientist with Science Directorate, NASA Langley Research Center, Hampton, VA, USA. He has developed algorithms for radiometric calibration, instrument line shape characterization, fast radiative transfer models, and atmospheric parameter retrievals for various instruments ranging from microwave to visible spectral range. He has served as a member on various government teams and performed collaborated work with international partners on remote sensing. He has developed a superfast principal-component-based radiative transfer model, which has been successfully applied to hyperspectral sensors, such as National Airborne Sounder Testbed Interferometer, Infrared Atmospheric Sounding Interferometer, Atmospheric InfraRed Sounder, Cross-track Infrared Sounder, and the Climate Absolute Radiance and Refractivity Observatory Pathfinder.

Dr. Liu was a recipient of numerous awards, such as the National Science Foundation Antarctic Service Award, the NASA Superior Accomplishment Award, the NASA Inventions and Contributions Board Awards, the NASA Exceptional Achievement Medal, and the NASA Exceptional Scientific Achievement Medal.

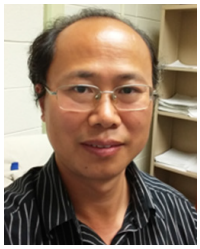

Qiguang Yang received the Ph.D. degree in optics from the Chinese Academy of Sciences, Beijing, China, in 1998.

He is currently a Senior Research Scientist with ADNET Systems Inc., Bethesda, MD, USA. His research interests include the development of fast and accurate principal-component-based radiative transfer model, hybrid stream radiative transfer model, hyperspectral remote sensing, and the application of satellite observations. The models he developed are fast and accurate for both thermal spectrum and reflected solar spectrum simulation in the cloudy atmosphere.

Jon Chris Currey received the M.S.E.E. degree in electronics and computer science from the University of Santa Clara, Santa Clara, CA, USA, in 1985.

He is currently the Data Manager of a team of software engineers at the NASA Langley Research Center, Hampton, VA, USA, responsible for developing the Climate Absolute Radiance and Refractivity Observatory (CLARREO) Pathfinder Inter-calibration Science Data System. CLARREO will be one the first NASA Earth Science missions to implement all science processing within the Cloud. Previously, he was the CALIPSO Data Manager responsible for developing the CALIPSO science data system. He was the PI for a NASA ROSES proposal from 2011 to 2015 focused on improving distributed processing capabilities for Earth science data systems.

Mr. Currey received the NASA Exceptional Achievement Medal for "developing and implementing an innovative data management system and science production software for the CALIPSO mission."

Aron D. Bartle received the M.S. degree in computer science from George Mason University, Fairfax, VA, USA, in 1999.

He is currently a Senior Software Engineer with Mechdyne Corporation, Marshalltown, IA, USA. His interests include scientific data processing using cloud-based services. He has implemented intercalibration algorithms and data processing pipelines for the Climate Absolute Radiance and Refractivity Observatory (CLARREO) Pathfinder mission that require from tens to hundreds of thousands of CPU-hours.

Adam Thurston received the B.S. degree in electrical engineering from the Harvey Mudd College, Claremont, CA, USA, in 2000.

He is currently a Senior Software Engineer with Mechdyne, Marshalltown, IA, USA. Past projects include the development of high bandwidth video processing systems and distributed graphics software. He currently supports the NASA Climate Absolute Radiance and Refractivity Observatory (CLARREO) Pathfinder project where the team is developing a lightweight serverless system to produce the L4 intercalibration products.

Natividad M. Smith received the M.S. degree in mechanical engineering from Old Dominion University, Norfolk, VA, USA, in 1996.

She is currently a Senior Research Scientist with Analytical Mechanics Associates, Inc., Hampton, VA. She has supported various NASA Langley Research Center projects with her primary work focused on the Clouds and the Earth's Radiant Energy System (CERES) project. Her research experience includes the development and validation of CERES angular directional models (ADMs), development of scientific algorithms and data analysis software for validation of Earth radiation budget data, and development and implementation of CERES instrument calibration and validation protocols.

Yolanda L. Shea received the B.S. degree in earth and atmosphere science from Cornell University, Ithaca, NY, USA, in 2007, and the Ph.D. degree in atmospheric and oceanic science from the University of Colorado at Boulder, Boulder, CO, USA, in 2012.

She has been a Research Scientist with the NASA Langley Research Center, Hampton, VA, USA, since 2012, with a focus on shortwave hyperspectral climate observations and is the Project Scientist of the Climate Absolute Radiance and Refractivity Observatory (CLARREO) Pathfinder (CPF) mission.

Dr. Shea was a recipient of several prestigious awards in her career, most notably the Presidential Early Career Award for Scientists and Engineers (PECASE) in 2019.

Rajendra Bhatt received the M.S. degree in electrical engineering from South Dakota State University, Brookings, SD, USA, in 2009, and the Ph.D. degree in electrical engineering from the University of Virginia, Charlottesville, VA, USA, in 2020.

Currently, he is supporting the Climate Absolute Radiance and Refractivity Observatory (CLARREO) Pathfinder (CPF) project with the NASA Langley Research Center, Hampton, VA, as the Deputy Project Scientist of intercalibration. Prior to joining CPF, he worked on the Clouds and the Earth's Radiance Energy System (CERES) project for 12 years, where he was primarily involved in developing techniques for in-flight calibration of geostationary and low earth-orbiting satellite imagers to assess their radiometric performance on orbit and ensure the usability of the satellite observations for climate studies.